Computer vision for improved estimates of SO_2 emission rates and plume dynamics

H. E. Thomas[a] and A.J. Prata[b,c]

[a] School of Earth Sciences, University of Bristol, Queen's Road, Bristol, BS8 1RJ, United Kingdom
[b]Visiting Scientist, Department of Atmospheric, Oceanic and Planetary Physics, University of Oxford, Parks Road, Oxford, OX1 3AN, United Kingdom.
[c]AIRES Pty Ltd, PO Box 156, Mt Eliza, Victoria, 3930, Australia.

ARTICLE HISTORY
Compiled October 19, 2017

ABSTRACT
Imaging cameras operating at ultra-violet (UV) and infrared (IR) wavelengths can measure sulfur dioxide (SO_2) gas path concentrations or slant column densities. These measurements are useful in a variety of applications including the monitoring of emissions from volcanoes and also emissions from stacks at industrial plants and on ships. The usefulness of these data is increased if the emission rates (or fluxes) of the gases can also be estimated. Here we present an optical flow algorithm that allows rapid and accurate estimates of emission rates using both UV and IR camera imagery sampling at around 1 Hz or higher. Examples are provided from measurements made at Turrialba volcano, Costa Rica and also at a ship in Hong Kong harbour. Other aspects of the properties of the fluid flow are also introduced, notably the divergence and the vorticity of the two-dimensional wind field. We demonstrate how the divergence can be used in a new method to calculate the emission rate and show how rotational effects observed in volcanic plumes and the resulting entrainment of ambient air affects plume rise and can be observed using vorticity. This is an important aspect for understanding the emplacement of gases and particles into the atmosphere that are subsequently transported by atmospheric winds, sometimes causing pollution episodes at long distances from the source.

KEYWORDS
Sulfur Dioxide, Remote Sensing, Optical Flow, UV Camera, IR Camera.

1. Introduction

Sulfur dioxide (SO_2) emissions to the atmosphere can have significant environmental effects from reduced air quality, ecosystem damage through acidic precipitation (affecting soils, water sources and the wildlife dependent on them) and also climatic influences through oxidation to sulfate particles. Sulfate aerosols reflect sunlight back into space and also act as cloud condensation nuclei (CCN), resulting in net cooling at the Earth's surface (e.g. Robock, 2000). Sulfur is commonly found in the biosphere and in fossil fuels such as crude oil and coal which typically contain 1% - 2% sulfur (S) by weight (Smith et al., 2011). Although anthropogenic emissions peaked in the early 1970s, emissions since 2000 have again risen

CONTACT H. E. Thomas. Email: helen.thomas@bristol.ac.uk

due to increased shipping, industrialisation and increases in transportation, particularly in developing countries (Smith et al., 2011). The recent revision of MARPOL Annex vi (http://www.imo.org/en/OurWork/environment/pollutionprevention/airpollution/pages/air-pollution.aspx) aims to limit exhaust pollution from ships and increases the need for efficient and accurate emissions monitoring. Natural sources of SO_2, such as volcanoes also contribute significantly to the global sulfur budget (Berresheim and Jaeschke, 1983) and can have large climatic impacts (Robock, 2000).

SO_2 is a well studied atmospheric species due to its unique spectral signature at ultraviolet (UV) and infrared (IR) wavelengths, facilitating its detection with remote sensing techniques (e.g. Galle et al., 2010). Emission rates from both natural and anthropogenic sources have traditionally been made from measurements with spectrometers e.g. Differential Optical Absorption Spectrometry (DOAS) (Platt and Stutz, 2008; Boichu et al., 2010; McGonigle et al., 2005; Rivera et al., 2011). McElhoe and Conner (1986) demonstrated the use of a portable UV sensitive video camera for SO_2 at industrial stacks. More recently, as technological developments have made UV camera CCD technology more portable and affordable, multi-spectral UV imaging cameras have become a commonly used tool for volcanic (Bluth et al., 2007; Mori and Burton, 2006; Kern et al., 2009; Platt et al., 2015, Burton et al., 2015) and industrial (Smekens et al., 2015) SO_2 quantification. Prata (2014) demonstrated how such a camera can be used to detect ship emissions of both SO_2 and particulates.

A key advantage of imaging cameras over spectrometers is that the plume speed may be calculated from a sequence of images, provided the geometry and locations of the camera and target are known. Previous studies have employed a number of methods to determine plume speed such as feature tracking (Bluth et al., 2007), cross-correlation (Nadeau et al., 2011) and edge detection (Lopez et al., 2013). Valade et al., (2014) have developed a method of plume tracking using filtering based on a temperature threshold and difference images. The software, known as *Plume Tracker*, is able to calculate the velocity of the leading edge along with other parameters such as acceleration and plume shape (Valade et al., 2014). As mass flux is defined as the rate of transfer of particles through a unit area and is calculated from the product of mass and velocity, it is therefore a vector quantity which is highly variable in both time and space. More recently, Peters et al., (2014) and Kern et al., (2015) have aimed to address this by demonstrating the use of optical flow modelling to determine plume speeds over the entire 2-dimensional plume surface from UV camera retrievals of volcanic SO_2.

2. Methods

In this work, we demonstrate an optical flow approach to determine motion at all points within an SO_2 image and demonstrate how this information may be utilised in better describing emission patterns and plume dispersion. New methods for calculation of SO_2 emission rates along with plume vorticity and divergence are also introduced.

2.1. *UV Cameras*

Ultraviolet imaging cameras have been used extensively by a number of research groups for more than ten years of volcanic SO_2 monitoring (e.g Mori and Burton, 2006; Bluth et al., 2007; Kern et al., 2009; Yamamoto et al., 2008). Measurements are typically made at two wavelengths, one between 300 and 320 nm where SO_2 absorbs radiation

and one at wavelengths longer than 320 nm (e.g. 325 nm) where SO_2 has little effect on absorption, which is used to correct for other species in the plume. Systems acquire images either using one sensor with rapidly changing filters (e.g Lübcke et al., 2012; Kern et al., 2010) or through using two collocated sensors, with each filter permanently attached to the instrument (e.g. Kantzas et al., 2010; Tamburello et al., 2011).

The retrieval of SO_2 slant column density (SCD) from UV measurements is described in Prata (2014). The retrieval methodology essentially assumes that the UV light intensity through the SO_2 plume is attenuated following the Beer-Bouguer-Lambert (BBL) law. An estimate of the incident or background light intensity is made by taking a horizontal transect through the plume and fitting a function (a quadratic is typically adequate) to this transect. The difference between the fitted function and the intensity in the plume is then assumed to be the absorbed light due to the plume and this in turn is related to the SCD of SO_2 in the plume. The BBL law assumes that the measured light intensity $I(\lambda)$, at wavelength λ, depends on the incident light intensity $I_0(\lambda)$ as:

$$I_\lambda = I_0(\lambda)\exp(-lk_{\rm s}(\lambda)), \tag{1}$$

where l is the slant column density (in units of molecules/cm^2 or g m^{-2}) and $k_{\rm s}(\lambda)$ is the absorption coefficient, which is a function of wavelength, λ. The incident light intensity is approximated from a Gaussian plus cubic fit (see Figure 1):

$$I_0 = a_0 \exp\left(-\frac{x-a_1}{a_2}\right)^2 + a_3 + a_4 x + a_5 x^2 + a_6 x^3, \tag{2}$$

where a_i, $i = 0, ...6$ are fitting coefficients and x is the pixel number. The function used is empirical and accounts for variations in the incident clear sky insolation and also for some of the aberrations due to the optics in the system. With knowledge of the absorption coefficient it is a simple matter to solve for l, noting that in practice the quantities are replaced by integrated quantities over a finite wavelength interval corresponding to the bandpass of the UV filter employed. This procedure works well in the absence of other substances (aerosols, gases or particles) that affect the light attenuation by the SO_2 plume. For volcanic plumes there may be particles, other gases and aerosols present that absorb UV light and in the case of ships, an important component of the plume is black carbon (bc) particles. These additional plume constituents can be strongly absorbing in UV light, as they are in visible light and can be corrected for by using a second filter at another wavelength and/or by using an additional UV spectrometer. The method used to correct for other interfering constituents follows Prata (2014). The correction procedure assumes that the absorption in the second channel is predominantly due to particulates (black carbon in the case of industrial emissions and ash in the case of volcanic emissions), while the absorption in the first channel is due to both SO_2 and light absorbing particulates. Employing the BBL law for the channel with central wavelength around 325 nm, the mass loading (g m^{-2}) of the interfering constituent (ic) with absorption coefficient $k_{\rm ic}$ is:

$$m_{\rm ic} = -\frac{1}{k_{\rm ic}(325)} \ln\left[\frac{I(325)}{I_0(325)}\right], \tag{3}$$

where the intensities $I(325)$, $I_0(325)$ are measured after and before the light enters

the plume and it is understood that a dark current value has been removed. At the wavelength where both SO_2 and the interfering constituent absorb, the mass loading due just to the interfering constituent is:

$$m_{\mathrm{ic}} = -\frac{1}{k_{\mathrm{ic}}(308)} \ln\left[\frac{I(308)}{I_0(308)}\right]. \tag{4}$$

Since the mass loading of the interfering constituent must be the same at both wavelengths,

$$\ln\left[\frac{I(308)}{I_0(308)}\right] = \frac{k_{\mathrm{s}}(308)}{k_{\mathrm{s}}(325)} \ln\left[\frac{I(325)}{I_0(325)}\right]. \tag{5}$$

Thus measurements of the intensities at wavelengths around 325 nm when combined with knowledge of the mass absorption coefficients of the interfering constituent can be used to estimate the logarithm of the ratio of intensities at the first wavelength (approximately 308 nm), where SO_2 is also absorbing. An estimate of the corrected SO_2 mass loading follows as:

$$m_{\mathrm{SO_2}} = -\frac{1}{k_{\mathrm{s}}(308)} \left\{ \ln\left[\left(\frac{I'(308)}{I'_0(308)}\right) \Big/ \left(\frac{I(325)}{I_0(325)}\right)^{\kappa} \right] \right\}, \tag{6}$$

where,

$$\kappa = \frac{k_{\mathrm{ic}}(308)}{k_{\mathrm{ic}}(325)}$$

and the I and I'_0 terms denote the measured light intensities exiting and entering the ship plume, without correction for soot at the two wavelengths used. Buffaloe et al. (2014) suggest that the mass absorption coefficient for black carbon at wavelength λ may be calculated from:

$$m_{\mathrm{s}}(\lambda) = k_{\mathrm{s}}(550) \left(\frac{550}{\lambda}\right), \tag{7}$$

where $k_{\mathrm{s}}(550) = 7.5 \pm 1.5$ m^2 g^{-1}. In the case of ash, Johnson *et al.* (2012) suggest a range for $k_{\mathrm{s}}(550)$ of 0.45 – 1.06 m^2 g^{-1} with a value of 0.6 m^2 g^{-1}, thought to be representative of distal ash clouds.

The data analysis proceeds on a pixel-by-pixel basis using the background intensity determined over a row or column of pixels, depending on the orientation of the plume under observation. For example, for a plume emitted from the funnel of a ship with low winds the transect through the plume is determined in the horizontal direction, along a line of pixels. If the plume is blown downwind and is now lying parallel to the horizontal then the transect is taken vertically, along a column of pixels. Some smoothing is usually applied to the final data to reduce noise and other artifacts of the processing.

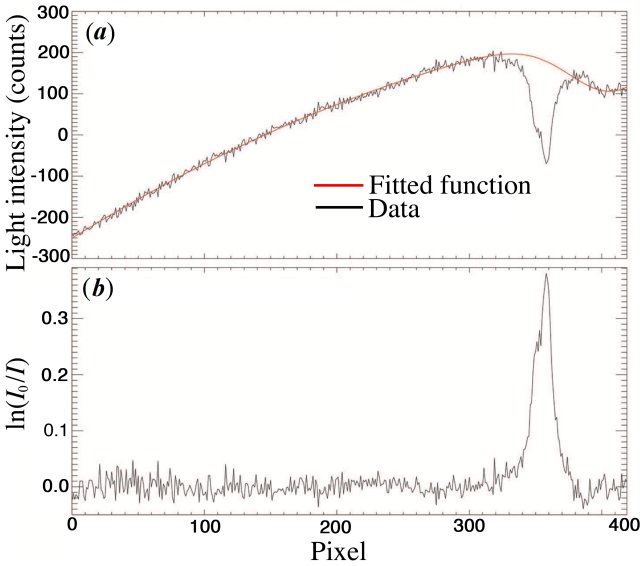

Figure 1. *Top-panel*: Horizontal variation of light intensity or counts across a ship plume (black line) and corresponding quadratic fit (red line). *Bottom-panel*: Difference (or residual) in light intensity between the measured and fitted intensities as a function of pixel number across the transect.

2.2. *IR Cameras*

With improvements in thermal detector technology and their subsequent affordability, thermal imaging cameras using uncooled microbolometer arrays are becoming an alternative method of quantifying volcanic SO_2 emissions from the ground (Lopez et al., 2015; 2013). As with UV technology, filters are used to select narrow wavebands where the spectral properties of volcanic species such as SO_2 and ash allow their discrimination from other atmospheric constituents such as water vapour. Unlike UV instruments, IR cameras can perform measurements at night-time as well as during the day and are thus advantageous where around-the-clock monitoring is required.

The retrieval of SO_2 from IR data is more complex than when using UV light. IR cameras essentially measure the emission or absorption of infrared light and this changes depending on the temperature of the target (the plume), the foreground radiation (emitters or absorbers in the light-of-sight and between target and camera) and background radiation from emitters behind the target. Ignoring, for the moment, the effects of substances between the plume and the camera (the foreground radiation), the plume may appear as an absorber or an emitter of IR radiation depending on the strength of the background radiation. This so-called thermal contrast (TC) is of a vital importance for estimating the slant column density: if the TC is small or zero then a retrieval is not possible. If it is positive (plume radiation is greather than background radiation) then the SO_2 gas emits radiation adding to the signal received at the camera. If the TC is negative (plume radiation is less than background radiation) then the SO_2 gas absorbs and reduces the signal received at the camera. For a plume with no SO_2 gas but other absorbers (e.g. water vapour) similar remarks can be made about the other absorbers. In most circumstances the plume has an excess temperature and appears warmer than the background and this effect may be due to emission from another gas (e.g. water vapour) or from heat derived from the energy source of the plume, for example the ships' engines in the case of a ship plume, or the heat generated by a volcano, in the case of a volcanic plume. By making measurements

at more than one wavelength (at least three are needed and four is preferable) it is possible to separate the effects of other absorbers (water vapour) and the effects due to the temperature of the plume and background.

This paper is not concerned with describing the IR retrieval methods and the interested reader should consult our earlier papers on this topic, see for example Prata and Bernardo (2014; 2009) and references therein. Here we have chosen to illustrate the emission rate determination from a volcanic plume where three narrowband channels have been used: one channel near 8.6 µm includes a strong SO_2 and a weaker water vapour absorption feature, a second channel near 11 µm is used to isolate the effects of water vapour (where no SO_2 absorption is present), while a third channel (at either 10 µm or 12 µm) permits an estimate of the plume temperature. The data were obtained from an uncooled microbolometer camera with a moving filter wheel. This arrangement has many advantages, not least the lower cost compared to using multiple, single-filter cameras. However there are some disadvantages, most notably the data at different wavelengths are not synchronous and the extra time required to move the filter and gather radiation introduces a longer time interval between retrievals resulting in a sampling rate close to 0.1 Hz rather than 1 Hz.

2.3. *Computer Vision and Optical Flow*

Computer vision is the scientific field of acquiring, processing and analysing data, transforming still or video imagery into either a decision or a new representation (Bradski and Kaehler, 2008). OpenCV is an open source computer vision library which provides the infrastructure to implement sophisticated computer vision techniques easily. The library is available in multiple distributions, including C and C^{++}, Python, Ruby and Matlab and can be run on a range of platforms. In this work, we used openCV for Python (available from *docs.opencv.org*) on Windows OS to implement a number of computer vision techniques for image analysis.

Optical flow is used in computer vision to determine the 2D distribution of the apparent velocity of the intensity value movement on the image plane. Optical flow algorithms calculate the displacement of brightness patterns between image frame pairs. *Dense optical flow* algorithms calculate the displacement for all pixels within an image, while *sparse optical flow* algorithms estimate displacement for a selected number of pixels within the image (Fleet and Weiss, 2006). If the time interval between the two images is known, along with the viewing geometry and optical setup, the displacement vectors may be converted into velocity vectors. For computation of optical flow, the following approximation is used:

$$I(x,t) \approx I(x + \mathrm{d}x, t + \mathrm{d}t), \tag{8}$$

where $I(x,t)$ is the spatiotemporal function of image intensity and x describes the spatial location within the image. The assumption is that intensity at time t and $t+\mathrm{d}t$ remains the same and is acceptable for plume sampling rates of around 0.1–1 Hz used here. Expansion of the above gives:

$$\nabla^\top \boldsymbol{I} \times \boldsymbol{v} + I_t = 0, \tag{9}$$

where $\nabla^\top \boldsymbol{I} = (I_x, I_y)^\top$ is the gradient (where I_x, I_y are the horizontal and vertical components respectively), I_t is the temporal derivative of $I(x,t)$ and $\boldsymbol{v} = (\boldsymbol{u}, \boldsymbol{v})^\top$ is the image velocity. However, just one linear constraint is insufficient to determine the

two-dimensional velocity, which is known as the *aperture problem* and so an additional constraint is needed (see later discussion).

The OpenCV library contains a number of optical flow algorithms including the popular Lucas-Kanade (Lucas and Kanade, 1981), which is an example of a *sparse method* and is one of the fastest optical flow implementations. This method was found to be effective at flow velocity determination on the plume edge where contrasts were greatest. It was however, ineffective in the central areas of the plume due to the relative homogeneity of the region. The Farnebäck method (Farnebäck, 2003), although slightly computationally slower, is a *dense method* and was found to be more robust for the SO_2 plume scenarios tested. The use of this method has been shown by Peters et al. (2014) to produce robust velocity vectors when applied to synthetic plumes and was computationally faster than the alternative DT-CWT method (Magarey and Kingsbury, 1998) .

The Farnebäck optical flow implementation (Farnebäck, 2003) uses a polynomial expansion method to approximate the neighbourhood (N_p) of each pixel (p), through a quadratic polynomial. In this method, the vector coefficients of the polynomial are found using a weighted least squares approach. From the exact quadratic polynomial:

$$f(\boldsymbol{x}) = \boldsymbol{x}^\top \mathbf{A} \boldsymbol{x} + \boldsymbol{b}^\top \boldsymbol{x} + c, \tag{10}$$

where $\boldsymbol{x} = [x, y]^\top$ is the vector containing the image coordinates, $\mathbf{A}$ is a symmetrical matrix, $\boldsymbol{b}$ a vector and c a scalar corresponding to the polynomial expansion coefficients, a new signal is constructed by applying a global displacement, $\boldsymbol{s}$ to yield:

$$f(\boldsymbol{x}) = f(\boldsymbol{x} - \boldsymbol{s}) = \boldsymbol{x}^\top \mathbf{A}' \boldsymbol{x} + \boldsymbol{b}'^\top \boldsymbol{x} + c', \tag{11}$$

where: $\mathbf{A'} = \mathbf{A}$, $\boldsymbol{b}' = \boldsymbol{b} - 2\mathbf{A}\boldsymbol{s}$, and $c' = \boldsymbol{s}^\top \mathbf{A} \boldsymbol{s} - \boldsymbol{b}^\top \boldsymbol{s} + c$.

Under the condition that $\mathbf{A}$ is non-singular, the displacement may be obtained from the above giving:

$$\boldsymbol{s} = -\frac{1}{2}\mathbf{A}^{-1}(\boldsymbol{b}' - \boldsymbol{b}) = \mathbf{A}^{-1}\Delta\boldsymbol{b}. \tag{12}$$

Because assuming the entire signal is a single polynomial is unrealistic (Farnebäck, 2003), the global polynomial expansion is replaced with local polynomial approximations to obtain the primary constraint where the global displacement is replaced with a spatially varying displacement field $\boldsymbol{d}(\boldsymbol{x})$:

$$\mathbf{A}(\boldsymbol{x})\boldsymbol{d}(\boldsymbol{x}) = \Delta b(\boldsymbol{x}). \tag{13}$$

Solving the above point-wise yields noisy results and so it is assumed that the optical flow varies slowly within a neighbourhood,N_p and $d(\boldsymbol{x})$ is found by computing $\mathbf{A}^\top\mathbf{A}, \mathbf{A}^\top\Delta\boldsymbol{b}$ and $\Delta\boldsymbol{b}^\top\Delta\boldsymbol{b}$ pointwise and averaging with a weighting function, w. The solution is obtained by finding the minima for:

$$\boldsymbol{d}(\boldsymbol{x}) = \left(\sum w\mathbf{A}^\top\mathbf{A})^{-1}\right)\sum w\mathbf{A}^\top\Delta\boldsymbol{b}. \tag{14}$$

(Farnebäck and Nordberg, 2002), to estimate displacement. The estimation uses a pyramidal approach, beginning at the most coarse level (for large motion detection)

down to the full image resolution level (where small motion is detected) by refining the estimates at each step.

2.4. *Conversion to emission rate*

The optical flow model provides values of $\boldsymbol{u}$ and $\boldsymbol{w}$ at spatial scales of a few metres (where $\boldsymbol{u} = \partial x/\partial t$ and $\boldsymbol{w} = \partial z/\partial t$) . With a single fixed-viewing imaging camera it is only possible to resolve the vector flow field in two dimensions (2D). Usually these are one horizontal direction and the vertical direction. We will first consider the general case in three-dimensional space, where the vector flow field is denoted as:

$$\boldsymbol{F} =< \boldsymbol{u}, \boldsymbol{v}, \boldsymbol{w} > . \tag{15}$$

Green's theorem states that the flux J (g s^{-1}) of material leaving the (closed) surface S, is

$$J = \oint_{\mathrm{S}} (\nabla \times \boldsymbol{F})\boldsymbol{n} \ \mathrm{dS}, \tag{16}$$

where $\boldsymbol{n}$ is a unit vector (pointing outwards from the surface). By Stoke's theorem this flux must be balanced by the change in sources and sinks within the cloud of volume V,

$$\oint_{\mathrm{S}} (\nabla \times \boldsymbol{F})\boldsymbol{n} \ \mathrm{dS} = \int\int\int_{\mathrm{V}} \nabla \boldsymbol{F} \ \mathrm{dV}. \tag{17}$$

Hence the divergence of the (3D) vector flow field provides a way to estimate the flux of mass leaving the plume in the absence of a background flow (a wind). The divergence can be calculated from estimates of the flow field:

$$\nabla \boldsymbol{F} = \frac{\partial \boldsymbol{u}}{\partial x} + \frac{\partial \boldsymbol{v}}{\partial y} + \frac{\partial \boldsymbol{w}}{\partial z}, \tag{18}$$

where x, y and z are Cartesian coordinates for the two horizontal and the vertical directions, respectively.

2.5. *Estimating the 3D field from the 2D field*

With one camera, flow in directions parallel to the line-of-sight of the camera cannot be determined. By using three or more cameras at different (fixed) positions it is possible in principle to estimate all components of the flow field and there are plans to utilise more cameras to develop tomographic images of dynamic plumes in the near future. For the 2D case, if we choose the x, y, z coordinates to be parallel to the $\boldsymbol{u}$, $\boldsymbol{v}$ and $\boldsymbol{w}$ wind directions, then the rotation matrix about the z-plane for camera axes x', y' and z' is:

$$\begin{bmatrix} x \\ y \\ z \end{bmatrix} = \begin{bmatrix} \cos\alpha & -\sin\alpha & 0 \\ \sin\alpha & \cos\alpha & 0 \\ 0 & 0 & 1 \end{bmatrix} \times \begin{bmatrix} x' \\ y' \\ z' \end{bmatrix}, \tag{19}$$

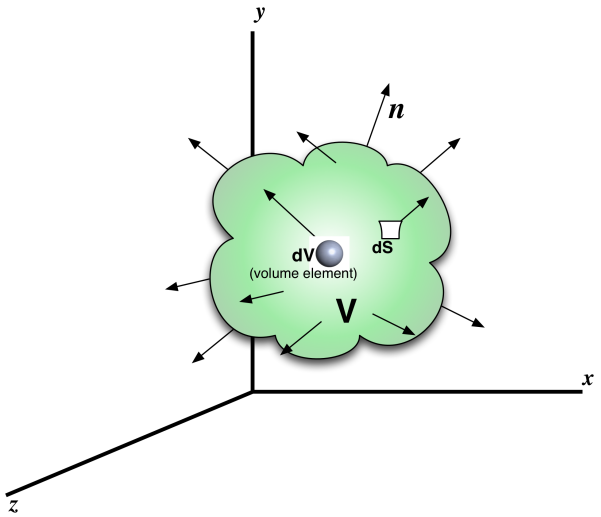

Figure 2. Schematic of plume, coordinate system and vector flow field. The unit vector $\boldsymbol{n}$ points outwards from a surface element dS on the surface of the plume of volume, V. A spherical volume element dV is used to calculate the divergence.

where the rotation is about the z-axis and α is the rotation angle. In most situations it is best to choose the z-axis in the direction of view of the camera, since motion in that plane cannot be detected. If we choose $\boldsymbol{w'}$ to be the component of the flow not observed, equation 19 becomes:

$$\nabla_{\mathrm{h}}\boldsymbol{F} = \cos\alpha\left(\frac{\partial \boldsymbol{u'}}{\partial x} + \frac{\partial \boldsymbol{v'}}{\partial y}\right) + \sin\alpha\left(\frac{\partial \boldsymbol{u'}}{\partial y} - \frac{\partial \boldsymbol{v'}}{\partial x}\right). \tag{20}$$

The component in the direction parallel to the camera viewing direction is undetermined and we use the subscript h to indicate that this is a 2D field. If it is possible to point the camera so that $\cos\alpha = 1.0$, then $\boldsymbol{F}$ is simply the horizontal component of the true wind field. Alternatively, the camera can be oriented so that the $\boldsymbol{v'}$ component is smallest. Both orientations are usually possible under field conditions.

The flux can be obtained directly from the divergence,

$$J = \sum_{i}^{N} \rho_i V_i \left\{ x\frac{\partial \boldsymbol{u}_i}{\partial x} + \frac{\partial \boldsymbol{v}_i}{\partial y} \right\}, \tag{21}$$

where N is the total number of surface elements, ρ_i is the concentration and V_i is a volume of an element chosen using a suitable sampling size, based on the spatial resolution of the image. In practice as the SCD (mass, m_i × area, A_i) is retrieved rather than the concentration, equation 21 is replaced by:

$$J = \sum_{i}^{N} m_i A_i \left\{ \frac{\partial \boldsymbol{u}_i}{\partial x} + \frac{\partial \boldsymbol{v}_i}{\partial y} \right\}. \tag{22}$$

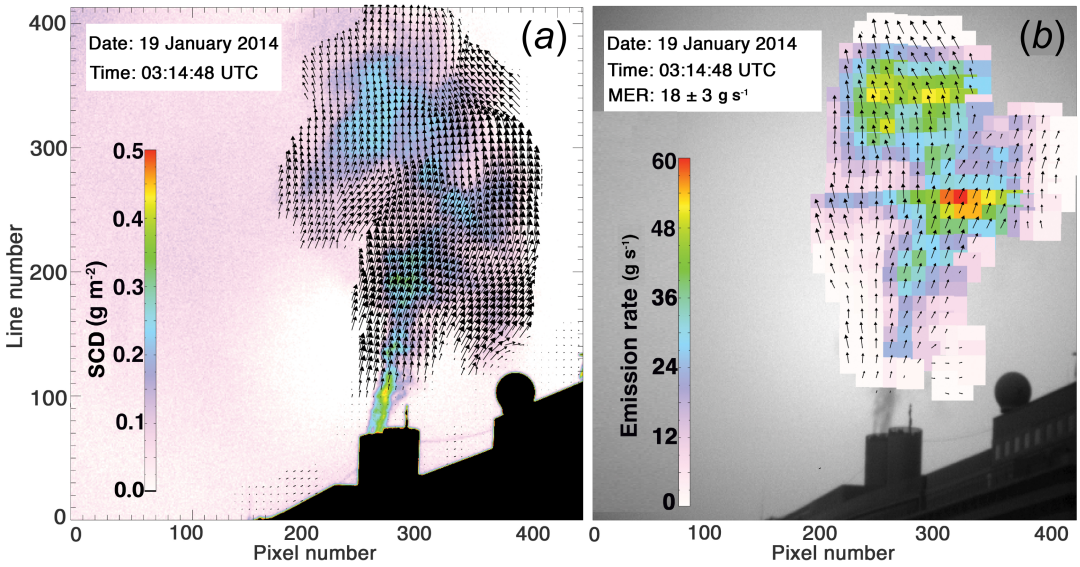

Figure 3. (a) SO_2 retrieval – slant column density (SCD) and (b) emission rates as measured at the Costa Victoria on January 19, 2014. The mean emission rate (MER) is also shown.

Stoke's theorem states that the flux out of a closed surface is equal to the sum of all sources in, minus the sum of all sinks out (Novotny and Straskraba, 2004). In other words, the outward flux of a vector through a closed surface is equal to the volume integral of the divergence over the region inside the surface. Therefore, by calculating the divergence of a plume and applying Green's theorem, the total flux leaving the surface (in this case, the plume edge) to the atmosphere can be derived. The calculation proceeds by dividing up the image into smaller segments (e.g. 5×5 pixels) and computing the right-hand-side of equation 22. The group size is adjustable, but if it is too small then the estimates tend to be noisy, while too large a group size tends to produce smoothed values. An example of the calculation of the SO_2 slant column density and corresponding emission rate for the Costa Victoria ocean liner at dock in Hong Kong harbour is shown in Figure 3.

To illustrate the difference between the two methods for calculating the emission rate (i.e. Green's theorem and the transect method) they are compared in Fig. 8 for the data shown in Fig. 3. This demonstrates that while the plume was relatively steady, the two methods match reasonable well, although later in the sequence where the plume was more energetic, the disparity between the two methods is much larger.

2.6. *Divergence*

In order to apply the above method to SO_2 camera data, the divergence must be calculated. Divergence, $\mathcal{D}$ is defined for two dimensional fluid flow as,

$$\mathcal{D} = \left(\frac{\partial \boldsymbol{u}}{\partial x} + \frac{\partial \boldsymbol{v}}{\partial y} \right). \tag{23}$$

This quantity is easily calculated using the optical flow retrievals as both the u and v components are known everywhere inside the plume. Divergence can be used to calculate the flux or emission rate using equation 22 and the theory described above.

An example of a divergence calculation is shown in Figure 4(b).

2.7. *Vorticity*

Another interesting parameter that may be derived from the optical flow data with SO_2 cameras is the vorticity. The camera measures two components of the flow field–the two wind components in the plane perpendicular to the viewing direction. With a single SO_2 camera it is not possible to fully resolve the wind field. Some extra information is needed in order to resolve the three dimensional wind field, for example a vertical view of the plume direction taken from a UAV or a high-resolution satellite sensor, or several cameras simultaneously viewing the same plume but from different vantage points. For this work we simply demonstrate how the vorticity can be computed, assuming that extra information is available from ancillary data.

The vertical component of the relative vorticity (ζ) is defined as:

$$\zeta = \lim_{A \to 0} \left(\oint \boldsymbol{v} \times l \right) A^{-1}, \tag{24}$$

where A is an area enclosed by a contour in a horizontal plane (in our case this is the plane perpendicular to the camera's viewing direction) and l an elemental distance along the contour. In practice, the relative vorticity is essentially the same as the absolute vorticity because at plume scales, the rotation of the earth is negligible. Taking the limit and assuming that the directional components of the 2-dimensional field are x and y and the wind field components are $\boldsymbol{u}$ and $\boldsymbol{v}$ yields:

$$\zeta = \left(\frac{\partial \boldsymbol{v}}{\partial x} - \frac{\partial \boldsymbol{u}}{\partial y} \right). \tag{25}$$

From Stoke's theorem it can be shown that the vertical component of the vorticity is a measure of the local angular velocity of the fluid. Vorticity is a very important aspect of fluid flow and is used in meteorology to study atmospheric weather patterns and is often more useful to describe fluid phenomena than the wind field itself. Conventionally positive vorticity is used to indicate clockwise rotation of the local fluid elements and negative vorticity corresponds to anti-clockwise rotation. The vorticity field for the plume shown in Figure 4(a) is quite flat, but there is an indication of positive vorticity on the right-hand edge of the plume and negative vorticity on the lower left-hand edge, suggesting that entrainment and mixing is occurring on these edges. There is no evidence that the plume is rotating and animations of a sequence of images confirms this (see supplementary material).

An example of the emergence of rotation in a plume can be seen in the formation of eddies or vortex rings (see Figure 5). These rings have been observed in the emissions from Mt Etna, Sicily and Stromboli as well as many other volcanoes. Ideally the component of interest is that parallel to the local vertical as is the case for the examples shown in Figure 5, where the vortex rotation is taking place in a horizontal plane about the local vertical (for cameras used from the ground, this vertical component is difficult to measure). Nevertheless the analysis presented here is quite general and applies to all two-dimensional wind fields. The presence of vorticity in plumes encourages entrainment of ambient air and ultimately causes dilution of the plume through mixing. Production of plumes by intense heating of the air for example in fires or in volcanic eruptions, can on occasion generate large amounts of vorticity resulting in structures

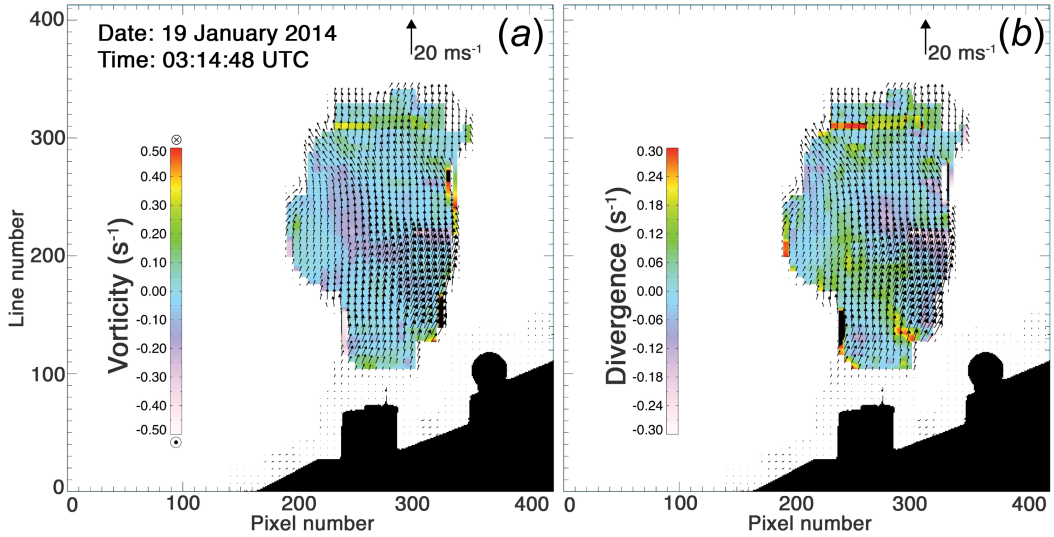

Figure 4. (a) Vorticity, and (b) Divergence for measurements at the Costa Victoria on January 19, 2014.

Figure 5. Examples of vortex rings forming above Mt Etna (a) and above a smoke plume (b). Credits: Tom Pfeiffer, fiboni.com.

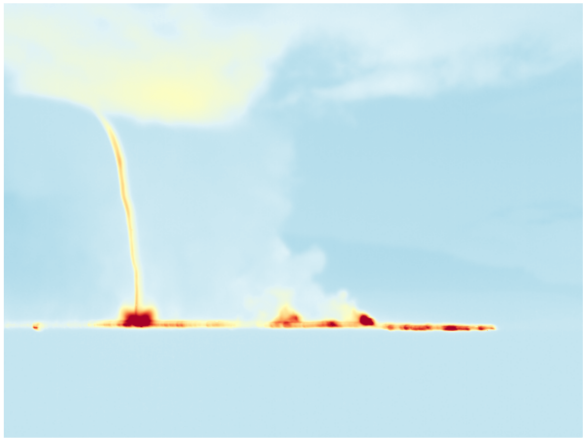

Figure 6. Thermal infrared (8.6 µm) image of a vortex column rising from the ground and intensely heated by erupting lava at Holuhraun, Iceland (Sept 2015). The vortex column is transporting material, mostly hot gases into the atmosphere. The vertical scale from the bottom of the vortex column to the top is about 1 km. The colours indicate brightness temperatures,where red is hottest and blue coolest. An short animation of the volcanic tornado can be found in the supplementary material.

comparable to tornadoes. An example of a vortex column generated by hot lava at the Holuhraun lava field from the eruption of Bárðarbunga in October 2014 and identified in ground-based filtered infrared camera imagery is shown in Figure 6. A vorticity calculation for these data is not possible because the camera was too distant (the image does not have sufficient spatial resolution) and because the rotation is in the horizontal plane as viewed from a camera looking vertically downwards. Such a viewing configuration can be achieved using a UAV-mounted camera or from an airborne or satellite platform.

Plumes from smoke stacks and funnels on ships tend to be less intensely heated and we expect that eddy generation would occur in all directions. Thus a horizontal view towards a rising plume is amenable to a vorticity analysis such as the example given in Figure 4(a). Positive vorticity is directed away from the camera (rotation in a clockwise sense) and negative towards the camera (anti-clockwise rotation). There is some structure in the vorticity field with a core of negative vorticity surrounded by smaller positive vorticity extending outwards to the plume edges.

3. Examples

For the example of the Costa Victoria (UV) and for an additional case study at Turrialba volcano, Costa Rica (IR), the Farnebäck optical flow algorithm was implemented using openCV to compute the velocity vectors between image pairs in each image sequence. The algorithm can be applied to either the retrieved SO_2 image sequence, or as was found for the Costa Victoria example, more robust results can be obtained when applied to the raw data (due to the higher level of image detail and contrast in the images). The derived velocity vectors, when applied to the SO_2 data enable the calculation of emission rate, divergence and vorticity.

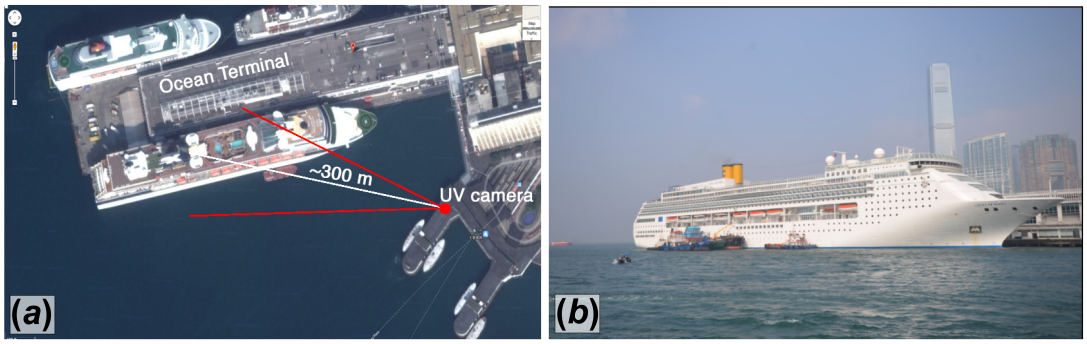

Figure 7. The Costa Victoria cruise ship and measurement location. a) Photograph showing the cruise ship, Costa Victoria at berth in Hong Kong and b) the location of the UV camera for these measurements.

3.1. *Example: Costa Victoria*

Cruise ship data were acquired while the vessel was at berth at the Ocean Terminal in Hong Kong as shown in Figure 7a. Measurements were acquired for just over 20 minutes between 03:23 and 03:45 UTC (11:23-11:45 local time) on 19 January 2014 from across the harbour, approximately 300 m distance (Figure 7b). The SO_2 retrieval can be seen in figure Figure 3(a) and (b) and the associated products derived from the optical flow technique in Fig.4(a) and (b).

Emission rates were calculated for two periods of time while the Costa Victoria was at dock but with some engines running. Means of emission rates for the two time periods are 17.6 and 16.2 g s^{-1} $\pm$4 g s^{-1}. These values are higher than SO_2 emissions from ships at sea reported by Hobbs et al. (2000) who found values from 3–12 g s^{-1}; although the values depend on the capacity of the engines, their efficiency and the fuel type used. For comparison we also calculated the emission rates from another (smaller) vessel, a container ship also at dock. The mean emission rate in this case was 0.8 g s $^{-1}\pm$ 0.3 g s^{-1}. This much smaller rate suggests that the ship was using auxiliary power at a low capacity. Emissions from these ships also contain particulates. These can be corrected using the off-band wavelength channel of the UV camera and after correction the emission rate of SO_2 can be reduced by as much as 20% of the rate estimated without correcting for particulates. These corrections are independent of the way the rates are calculated but do impact the amount of SO_2 gas estimated by the camera.

Figure 8 shows a subset of the Costa Victoria emissions data to illustrate the difference between the Green's theorem method of flux calculation and the more traditionally used transect method. This time period was chosen as the plume remained vertical and therefore the horizontally drawn transect would be valid. Within this period, three phases of plume behaviour are visible: relatively steady with small emission fluctuations (start - 16.0 minutes), a steady plume (16.0 - 16.4 minutes) and finally a period of more energetic pulses (16.4 minutes - end). The flux calculation using the transect method was performed using the mean of the wind speed along the transect line as it is usual to assume just one speed. The grey shaded region shows the standard deviation in emission rate given by variability in wind speed across the transect line. No correction for particulates was made in this case (as only on-band images were acquired for this period to maximise frame rate) and so these estimates are likely biased high by up to 20%.

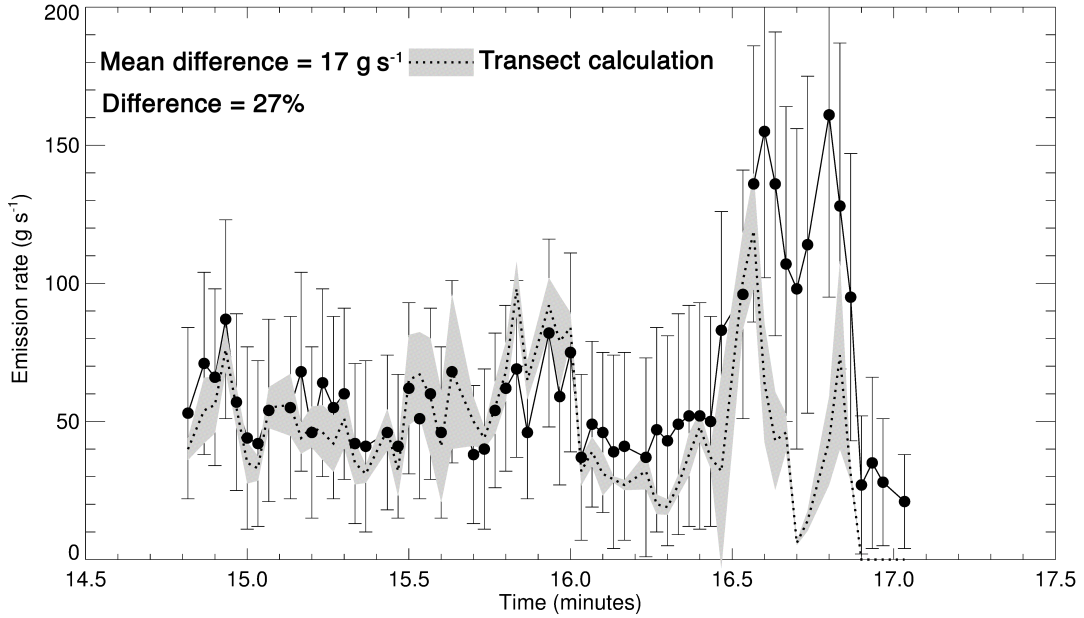

Figure 8. Costa Victoria emission rates estimated using a UV camera for the Costa Victoria while at dock using Green's theorem with a transect calculation shown for comparison (dotted line). The shaded region indicates the standard deviation of the transect method based on the variability in wind speed along the transect. Error bars represent the variability of calculated emission rate for each sub-region in the image.

3.2. *Example: Turrialba Volcano*

Data from Turrialba were acquired during a field campaign on 19th January 2011, between 04:21 and 07:45 UTC (22:21, 18 January to 01:45 local time on 19 January) from the Turrialba Lodge Hotel (see Figure 3.2). Data were acquired using a custom built infrared imaging camera (similar to that described by Prata and Bernardo, 2014), enabling the plume dynamics during the night-time to be measured. One limitation with the camera is that due to the single camera design and rotating filter wheel, the time interval between image sets is typically on the order of 10 - 20 seconds (depending on the number of filter channels chosen and the shutter interval) (Prata and Bernardo, 2014). This results in large displacements between successive frames with large and highly variable SO_2 concentrations. As a result of the large time difference between frames, the Farnebäck algorithm using the raw data alone failed (Farnbebäck, 2003). In order to calculate velocity vectors in this case, we use a feature based approach whereby a Sobel operator was applied to the image sequence prior to the optical flow algorithm implementation (Nourani-Vatani et al., 2012) to enhance the contrast between the main plume features in the image. This was found to improve the reliability of the algorithm and reduce additional effects from background noise and other moving objects in the frame (such as meteorological clouds) when retrieving the velocity vectors shown in Figure 10.

Turrialba is a large emitter of SO_2 with periods when emissions can be very high, up to 2 kilotonnes per day (de Moor et al., 2016; Xi et al., 2016). This variability seems to be reflected at many time scales from years, months and days down to several minutes. Our data show periods of tens of minutes when the volcano is quiet followed by periods of very high emissions. Consequently to characterise and measure the SO_2

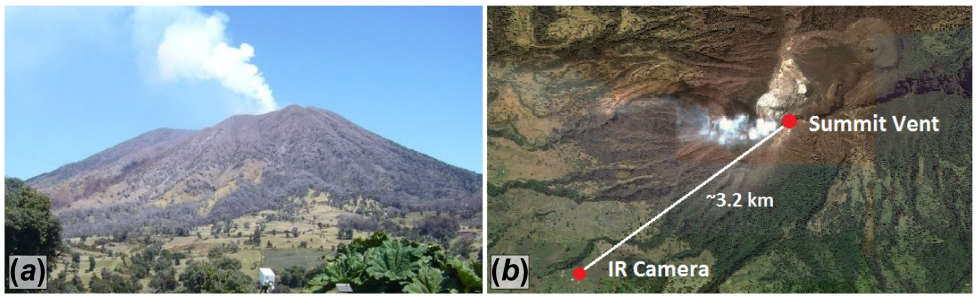

Figure 9. a) Photograph showing the view of Turrialba volcano, Costa Rica from the measurement location (taken approximately four hours after data shown here were acquired) and b) aerial view showing relative locations of the volcano summit and measurement location. (Aerial image from Google earth, acquired January 24 2011, ©2017 DigitalGlobe, ©2017 Europa Technologies).

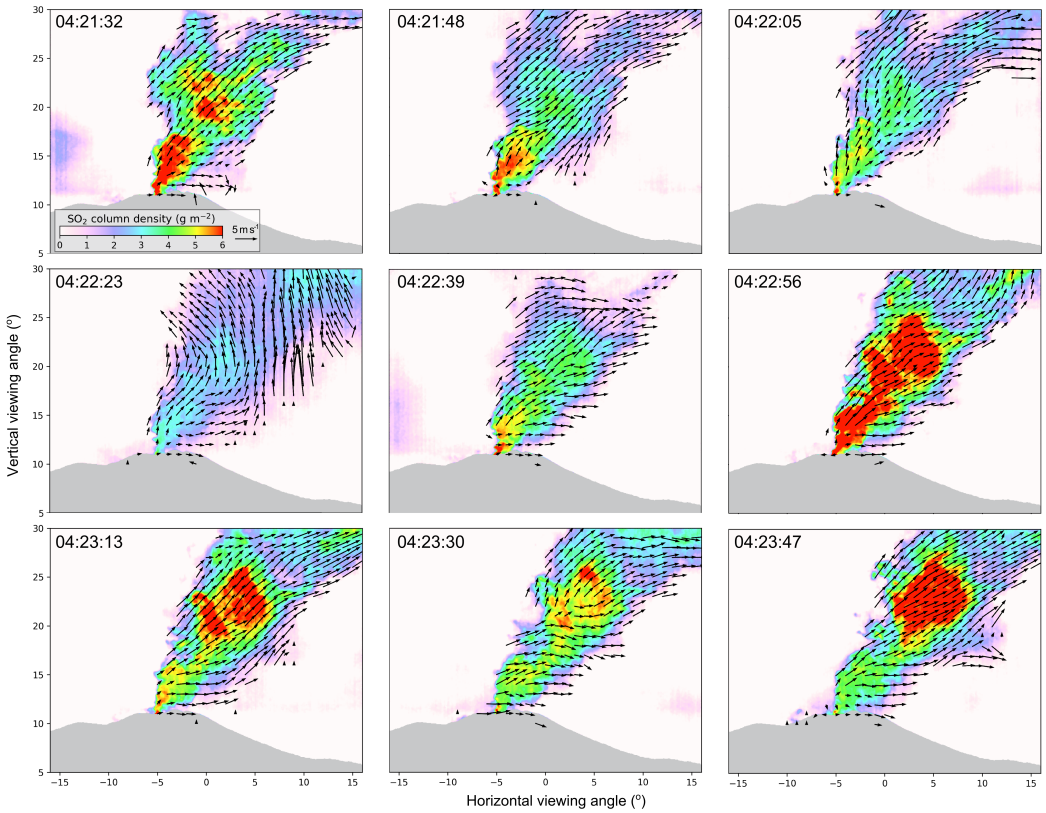

Figure 10. Retrieved SO_2 column density and velocity vectors for Turrialba volcano, Costa Rica. Geometry allows the calculation of plume speed from the vectors, which averaged at 4.4 m s^{-1}. Times are given in UTC where local time in Costa Rica is UTC-6. (See supplementary materials for an animation of the entire image sequence.

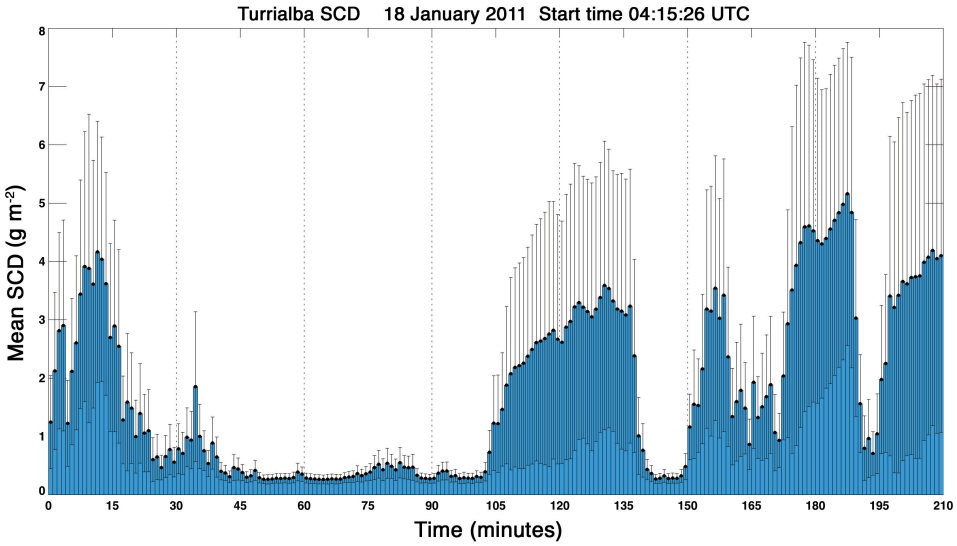

Figure 11. Time series of the mean of the slant column densities of the Turrialba SO_2 emissions using the infrared camera. The black lines indicate the variability of the SCD as measured by the standard deviation.

emissions from Turrialba it is necessary to cover a large range of time scales and include nighttime periods of activity. Figure 11 shows the infrared retrievals of the SCD over a period of approximately three hours during the night. There is a period of around one hour (minute 30 to minute 90) when the SCDs are low and several periods lasting tens of minutes when SCDs exceed 2 g m^{-2}. To estimate the emission rate, as before, the optical flow algorithm was used to determine flow vectors and then the divergence was computed and finally the emission rate from equation 22 and multiplication with the SCD. To illustrate the results and compare them with the traditional transect method, (Fig. 12) shows a short period of data (about five minutes) when the volcano was active and emissions high. Emissions were also evaluated for three transects taken across the plume illustrated by the dashed line (half-way up the plume); dotted line (closer to the vent) and dot-dashed line (nearer the top of the plume). The mean winds determined at these heights from the optical flow were used. What is noticeable is that depending on exactly where the transect is taken, results can differ markedly (as was also observed by Smekens et al. 2015) . The flux method (solid line) appears to represent an average flux over the whole plume and the transect values fall within the variability of the emission rates determined by the flux method. It is also apparent that puffs in the emissions are captured at the sampling rate used (10–20 s) and this suggests that if representative emission rates are to be determined, then care must be taken in deciding on a sampling rate. Too short and turbulent puffs may bias the results; too long and important highly concentrated SO_2 puffs may be missed. For this case, during this period it appears that sampling at 10–30 s is appropriate. A long animation of the emissions from Turrialba as determined by the infrared camera is included in Supplementary Materials.

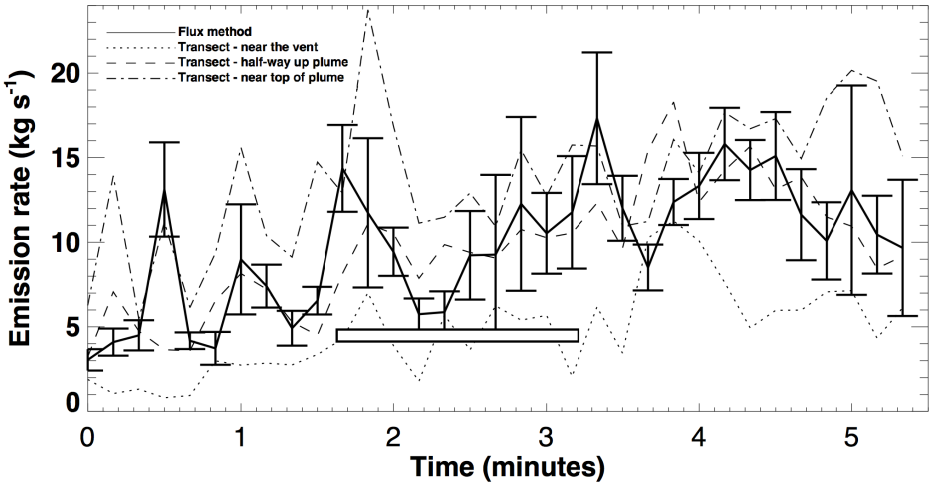

Figure 12. Emission rates for a period of approximately five minutes when Turrialba was very active. The solid black line is the emission rate determined from the integral flux method, with error bars to represent the variability of emission rate across regions of the image. Also shown are the results using the transect method. Error bars are indicated for the flux method. Emission rates are often quoted in tonnes of SO_2 per day. 1 kg s^{-1} = 0.0864 kilotonnes per day.

4. Conclusions

Imaging cameras operating at UV and IR wavelengths are becoming more affordable and useful in a variety of geophysical situations including safe monitoring of volcanic emissions. There are also important industrial applications including measuring SO_2 emissions from ships and from industrial stacks. Algorithms have been developed to determine slant column densities of SO_2 in plumes and because of the rapid imaging capability, optical flow techniques can be utilized to derive an estimate of the velocity field. In turn, a number of additional products can be derived including the divergence which can be used to compute the SO_2 emission rate. The technique allows flux to be calculated at all locations within the image, thus highlighting the spatial and temporal disparities in emission rates from volcanoes. In particular, optical flow demonstrates that regions of high flux may not necessarily correspond to those with the highest concentrations and the wide variability of flux with time can also be displayed more easily. Optical flow algorithms present a method of automating the computation of plume velocity, thus leading towards automated fluxes from imaging cameras which had not been possible with some previous methods. This is a first step towards using imaging cameras for continuous gas flux monitoring. We have also demonstrated how additional products, such as the vorticity can be derived using imaging camera data. As camera data become more widely available, and in particular from campaigns where multiple cameras are used at different viewing geometries and directions, calculations of the vorticity will enable insights into plume turbulence and entrainment dynamics.

Disclosure statement

The authors declare that they have no competing interest.

Funding

This work was partly supported by EU Seventh Programme for research, technological development and demonstration under grant agreement No. 308377 (FUTUREVOLC project) and NASA grant NNX08AF80G.

Notes on contributor(s)

All authors collected data at Turrialba and FP collected data in Hong Kong. HT designed and developed the optical flow procedure and performed the analysis. FP performed the emission rate, vorticity and divergence analysis. The IR and UV cameras were developed by FP in collaboration with Dr Cirilo Bernardo. All authors were involved in the construction, reading and approval of the final manuscript.

Acknowledgements

The authors would like to thank the participants and organisers of the PASI Workshop, Costa Rica 2011, who assisted us with logistics and data collection. Billy Cheung of the Environmental Protection Department of the Hong Kong Government provided support for the measurements in Hong Kong harbour. Kerstin Stebel and the Norwegian Institute for Air Research (NILU) are thanked for allowing us use of the UV and IR cameras. Cirilo Bernardo contributed to the design and development of the IR and UV cameras. The Icelandic Meteorological Office and members of the FUTUREVOLC team are thanked for support in collecting the Holuhraun data. Finally, we thank both reviewers for their insightful comments which significantly improved the manuscript.

References

Berresheim, H., and W. Jaeschke. 1983. "The contribution of volcanoes to the global atmospheric sulfur budget." *Journal of Geophysical Research: Oceans* 88 (C6): 3732–3740. http://dx.doi.org/10.1029/JC088iC06p03732.

Bluth, G.J.S., J.M. Shannon, I.M. Watson, A.J. Prata, and V.J. Realmuto. 2007. "Development of an ultraviolet digital camera for volcanic SO_2 imaging." *J. Volcanol. Geotherm. Res.* 161 (1-2): 47–56.

Boichu, M., C. Oppenheimer, V. Tsanev, and P. R. Kyle. 2010. "High temporal resolution SO_2 flux measurements at Erebus volcano, Antarctica." *Journal of Volcanology and Geothermal Research* 190 (3): 325–336.

Bradski, G., and A. Kaehler. 2008. *Learning OpenCV: Computer vision with the OpenCV library*. O'Reilly Media, Inc.

Buffaloe, G. M., D. A. Lack, E. J. Williams, D. Coffman, K. L. Hayden, B. M. Lerner, S.-M. Li, et al. 2014. "Black carbon emissions from in-use ships: a California regional assessment." *Atmospheric Chemistry and Physics* 14 (4): 1881–1896. https://www.atmos-chem-phys.net/14/1881/2014/.

Burton, M.R., F. Prata, and U. Platt. 2015. "Volcanological applications of SO2 cameras." *Journal of Volcanology and Geothermal Research* 300 (Supplement C): 2 – 6. http://www.sciencedirect.com/science/article/pii/S0377027314002935.

Farnebäck, G. 2003. "Two-frame motion estimation based on polynomial expansion." In *Image Analysis*, 363–370. Springer.

Farnebäck, G., and K. Nordberg. 2002. "Motion Detection in the WITAS Project." In *Swedish Symposium on Image Analysis (SSBA) : Lund*, 99–102.

Fleet, D., and Y. Weiss. 2006. "Optical flow estimation." In *Handbook of Mathematical Models in Computer Vision*, 237–257. Springer.

Galle, B., M. Johansson, Y. Rivera, C.and Zhang, M. Kihlman, C. Kern, T. Lehmann, U. Platt, S. Arellano, and S. Hidalgo. 2010. "Network for Observation of Volcanic and Atmospheric Change (NOVAC) - A global network for volcanic gas monitoring: Network layout and instrument description." *Journal of Geophysical Research: Atmospheres* 115 (D5).

Hobbs, Peter V., Timothy J. Garrett, Ronald J. Ferek, Scott R. Strader, Dean A. Hegg, Glendon M. Frick, William A. Hoppel, et al. 2000. "Emissions from Ships with respect to Their Effects on Clouds." *Journal of the Atmospheric Sciences* 57 (16): 2570–2590. https://doi.org/10.1175/1520-0469(2000)057<2570:EFSWRT>2.0.CO;2.

Johnson, B., K. Turnbull, P. Brown, R. Burgess, J. Dorsey, A. J. Baran, H. Webster, et al. 2012. "In situ observations of volcanic ash clouds from the FAAM aircraft during the eruption of Eyjafjallajkull in 2010." *Journal of Geophysical Research: Atmospheres* 117 (D20): n/a–n/a. http://dx.doi.org/10.1029/2011JD016760.

Kantzas, E.P., A.J.S. McGonigle, G. Tamburello, A. Aiuppa, and R.G. Bryant. 2010. "Protocols for UV camera volcanic SO_2 measurements." *Journal of Volcanology and Geothermal Research* 194 (1): 55–60.

Kern, C., T. Deutschmann, L. Vogel, M. Wöhrbach, T. Wagner, and U. Platt. 2009. "Radiative transfer corrections for accurate spectroscopic measurements of volcanic gas emissions." *Bull. Volcanol.* 72 (2): 233–247.

Kern, C., F. Kick, P. Lübcke, L. Vogel, M. Wöhrbach, and U. Platt. 2010. "Theoretical description of functionality, applications, and limitations of SO_2 cameras for the remote sensing of volcanic plumes." *Atmospheric Measurement Techniques Discussions* 3 (1): 531–578.

Kern, C., J. Sutton, T. Elias, L. Lee, K.Kamibayashi, L. Antolik, and C. Werner. 2015. "An automated SO_2 camera system for continuous, real-time monitoring of gas emissions from Kilauea Volcano's summit Overlook Crater." *Journal of Volcanology and Geothermal Research* 300: 81 – 94. http://www.sciencedirect.com/science/article/pii/S0377027314003783.

Lopez, T., D. Fee, F. Prata, and J. Dehn. 2013. "Characterization and interpretation of volcanic activity at Karymsky Volcano, Kamchatka, Russia, using observations of infrasound, volcanic emissions, and thermal imagery." *Geochemistry, Geophysics, Geosystems* 14 (12): 5106–5127.

Lopez, T., H.E. Thomas, A.J. Prata, A. Amigo, D. Fee, and D. Moriano. 2015. "Volcanic plume characteristics determined using an infrared imaging camera." *Journal of Volcanology and Geothermal Research* 300: 148 – 166. http://www.sciencedirect.com/science/article/pii/S0377027314003837.

Lübcke, P., N. Bobrowski, S. Illing, C. Kern, J. M. Alvarez Nieves, L. Vogel, J. Zielcke, H. Delgado Granados, and U. Platt. 2012. "On the absolute calibration of SO_2 cameras." *Atmospheric Measurement Techniques Discussions* 5 (5): 6183–6240. http://www.atmos-meas-tech-discuss.net/5/6183/2012/.

Lucas, B. D., and T. Kanade. 1981. "An Iterative Image Registration Technique with an Application to Stereo Vision." In *IJCAI*, 674–679.

Magarey, J., and N. Kingsbury. 1998. "Motion estimation using a complex-valued wavelet transform." *IEEE Transactions on Signal Processing* 46 (4): 1069–1084.

McElhoe, H.B., and W.D. Conner. 1986. *Remote measurement of sulfur dioxide emissions using an ultraviolet-light-sensitive video system.* Taylor & Francis.

McGonigle, A. J. S., S. Inguaggiato, A. Aiuppa, A. R. Hayes, and C. Oppenheimer. 2005. "Accurate measurement of volcanic SO_2 flux: Determination of plume transport speed and integrated SO_2 concentration with a single device." *Geochemistry, Geophysics, Geosystems* 6 (2). http://dx.doi.org/10.1029/2004GC000845.

Mori, T., and M. Burton. 2006. "The SO_2 camera: A simple, fast and cheap method for ground-based imaging of SO_2 in volcanic plumes." *Geophys. Res. Lett.* 33 (24): L24804.

Nadeau, P. A., J.L. Palma, and G.P. Waite. 2011. "Linking volcanic tremor, degassing, and eruption dynamics via SO_2 imaging." *Geophysical Research Letters* 38 (1).

Nourani-Vatani, N., P.V.K. Borges, and J.M. Roberts. 2012. "A study of feature extraction algorithms for optical flow tracking." In *Proc. Australian Conf. Robotics and Automation*, .

Novotny, A., and I. Straskraba. 2004. *Introduction to the Mathematical Theory of Compressible Flow*. Oxford University Press.

Peters, N., A. Hoffmann, T. Barnie, M. Herzog, and C. Oppenheimer. 2014. "Use of motion estimation algorithms for improved flux measurements using SO_2 cameras." *Journal of Volcanology and Geothermal Research* –. http://www.sciencedirect.com/science/article/pii/S0377027314002807.

Platt, Ulrich, Peter Lbcke, Jonas Kuhn, Nicole Bobrowski, Fred Prata, Mike Burton, and Christoph Kern. 2015. "Quantitative imaging of volcanic plumes Results, needs, and future trends." *Journal of Volcanology and Geothermal Research* 300: 7 – 21. http://www.sciencedirect.com/science/article/pii/S0377027314003047.

Prata, A. J. 2014. "Measuring SO_2 ship emissions with an ultraviolet imaging camera." *Atmospheric Measurement Techniques* 7 (5): 1213–1229. http://www.atmos-meas-tech.net/7/1213/2014/.

Prata, AJ, and C Bernardo. 2009. "Retrieval of volcanic ash particle size, mass and optical depth from a ground-based thermal infrared camera." *Journal of Volcanology and Geothermal Research* 186 (1): 91–107.

Prata, A.J., and C. Bernardo. 2014. "Retrieval of sulphur dioxide from a ground-based thermal infrared imaging camera." *Atmospheric Measurement Techniques Discussions* 7 (2): 1153–1211.

Rivera, C., G. Sosa, H. Wohrnschimmel, B.de Foy, M. Johansson, and B.Galle. 2011. "Tula Industrial Complex (Mexico) Emissions of SO_2 and NO_2 During the MCMA 2006 Field Campaign Using a Mobile Mini-DOAS System." In *Industrial Chemistry*, edited by William Hunter Jr Harold H. Trimm, Chap. 4, 56–74. Oakville, Canada: Apple Academic Press Press.

Robock, A. 2000. "Volcanic eruptions and climate." *Reviews of Geophysics* 38 (2): 191–219.

Smekens, J.-F., M. R. Burton, and A. B. Clarke. 2015. "Validation of the SO_2 camera for high temporal and spatial resolution monitoring of SO_2 emissions." *Journal of Volcanology and Geothermal Research* 300: 37 – 47. http://www.sciencedirect.com/science/article/pii/S0377027314003126.

Smith, S. J., J. van Aardenne, Z. Klimont, R. J. Andres, A. Volke, and S. Delgado Arias. 2011. "Anthropogenic sulfur dioxide emissions: 1850–2005." *Atmospheric Chemistry and Physics* 11 (3): 1101–1116. http://www.atmos-chem-phys.net/11/1101/2011/.

Tamburello, G., A.J.S. McGonigle, E.P. Kantzas, and A. Aiuppa. 2011. "Recent advances in ground-based ultraviolet remote sensing of volcanic SO_2 fluxes." *Annals of Geophysics* 54 (2).

Valade, S.A., A.J.L. Harris, and M. Cerminara. 2014. "Plume Ascent Tracker: Interactive Matlab software for analysis of ascending plumes in image data." *Computers and Geosciences* 66 (0): 132 – 144.

Yamamoto, H., I.M Watson, J.C. Phillips., and G.J. Bluth. 2008. "Rise dynamics and relative as distribution in vulcanian eruption plumes at Santiaguito Volcano, Guatemala, revealed using an ultraviolet imaging camera." *Geophys. Res. Lett.* 35: L08314.